Chinese Chemical Letters 35 (2024) 109268

Contents lists available at ScienceDirect

Chinese Chemical Letters

journal homepage: www.elsevier.com/locate/cclet

Heterogeneous bimetallic oxides/phosphides nanorod with upshifted d band center for efficient overall water splitting

Ji Chen[a], Yifan Zhao[a], Shuwen Zhao[a], Hua Zhang[a,*], Youyu Long[a], Lingfeng Yang[a], Min Xi[a], Zitao Ni[a,*], Yao Zhou[b,d,*], Anran Chen[a,c,*]

[a] School of Materials and Energy, Yunnan University, Kunming 650091, China
[b] School of Engineering, The University of Edinburgh, South Bridge, Edinburgh EH89YL, United Kingdom
[c] Electron Microscopy Center, Yunnan University, Kunming 650091, China
[d] School of Internet of Things Engineering, Jiangnan University, Wuxi 214122, China

ARTICLE INFO

Article history:
Received 17 July 2023
Revised 24 October 2023
Accepted 31 October 2023
Available online 4 November 2023

Keywords:
Hydrogen evolution reaction
Bimetallic oxides
Bimetallic phosphides
Overall water splitting
Solar-to-hydrogen efficiency

ABSTRACT

Electrocatalytic water splitting is the most directly available route to generate renewable and sustainable hydrogen. Here, we report the design of a composite material in which arrays of square pillar-like $NiMoO_4$ nanorods coated with N, P-doped carbon layers are uniformly contained in numerous nested nanoparticle structures. The catalysts have superior catalytic activity, requiring only 59 mV and 187 mV for HER and OER to attain a current density of 10 mA/cm^2, respectively. The assembled two-electrode electrolytic cell required a voltage of 1.48 V to reach 10 mA/cm^2, along with excellent long-term stability. Theoretical calculations reveal that electrons aggregate and redistribute at the heterogeneous interface, with the d-band centers of the Ni and Fe atoms being positively shifted compared to the Fermi level, effectively optimizing the adsorption of intermediates and reducing the Gibbs free energy, thus accelerating the catalytic process. Meanwhile, an integrated solar-driven water-splitting system demonstrated a high and stable solar-to-hydrogen efficiency of 18.20%. This work provides new possibilities for developing non-precious metal-based bifunctional electrocatalysts for large-scale water splitting applications.

With the increase in problems associated with resources and the environment, such as the emissions of sulfur oxides, nitrogen oxides, and greenhouse gasses, new energy options are needed to replace traditional fossil energy sources [1,2]. Compared with other fuels, hydrogen energy has a high energy density, and only water is the product after combustion, which is considered the most promising energy way in the future [3–5]. Clean hydrogen fuel can be produced *via* water splitting driven by harvesting renewable energy sources (solar, *etc.*), which can convert electrical energy to chemical energy and can be stored and used for ammonia production, petroleum refining, coke/iron production, fuel cell-powered vehicles, and residential purposes [6–9]. Free hydrogen is not a naturally occurring resource and must be synthesized. Currently, pure hydrogen is produced by three methods: methane steam reforming, coal gasification, and water electrolysis [10,11]. However, the first two methods require burning large amounts of fossil fuels, aggravating the energy crisis and environmental pollution. Electrocatalytic water splitting is currently the most directly available route to generate renewable and sustainable hydrogen; here, water is the only raw material, enabling a tight hydrogen cycle with no carbon emissions and no requirement for external chemical reagents [12].

In alkaline environments, the electrochemical water splitting process consists of two half-reactions, including hydrogen ions capture electrons at the cathode, in a reaction termed the hydrogen evolution reaction (HER), and hydroxyl ions lose electrons at the anode, in a reaction termed the oxygen evolution reaction (OER) [13–17]. Numerous studies have focused on optimizing these two important reactions to provide an efficient catalytic process and a reduced activation barrier, which is expected to boost the HER and OER simultaneously. It is thus compelling to develop an advanced bifunctional catalyst to replace the conventional single catalyst, leading to promoted activity and lower overpotentials in the overall water-splitting process. However, if there is an incompatibility between the two different catalysts used in a given system, the result will be inefficient water-splitting activity [18–21].

Among the developments in catalysis, Hammer and Nørskov developed what is perhaps the most famous theory in heterogeneous catalysis, known as the d-band theory. In theory, the d-band center can be used as a first-order descriptor of the propensity of a

---

* Corresponding authors.
E-mail addresses: zhanghua1226@mail.ynu.edu.cn (H. Zhang), nizitao@mail.ynu.edu.cn (Z. Ni), Yao.Zhou@ieee.org (Y. Zhou), anran@ynu.edu.cn (A. Chen).

https://doi.org/10.1016/j.cclet.2023.109268

transition metal to bind to adsorbates: the higher the d-band center, the stronger the binding [22,23]. A transition metal phosphide (TMP) system is increasingly attractive with its interesting physicochemical properties, including distinct electrical conductivity, polytropic compositions, improved reaction kinetics, and tunable d-band center, making it potentially advantageous and particularly suitable for the overall water-splitting process [24–26]. Various strategies and TMP-based catalysts have been designed to tailor the intrinsic properties and catalytic activity for the overall reaction [27,28]. The combination of amorphous and crystalline $NiCoP_x$ and surface-oxidized metal (oxygen) hydroxides have been shown to exhibit significant OER activity. Popczun *et al.* highlighted that preparations of Ni_2P with high-density (001) facets achieve excellent performance in acidic media [25]. Very recently, Li *et al.* indicated that phosphorus-rich CoP_2 could exhibit an enhanced performance compared to metal-rich TMP-based materials [29]. Ding *et al.* embedded FeP heterostructures into $Co(OH)_2$ and showed strong interactions at the FeP/$Co(OH)_2$ heterostructure interface, leading to enhanced catalytic activity by charge redistribution calculations and density of states (DOS) [30]. Zhang and his colleagues synthesized pod-like heterogeneous structures in which the carbon layer acts as a protective layer, thereby improving catalytic activity and durability [31]. Liu *et al.* reported that Ni_2P–NiP_2 heterostructures display smaller ΔG_{H^*} values compared to pure compounds [32]. Therefore, the construction of heterogeneous interfaces leads to the optimization of the valence electron state of the active center, resulting in the improvement of the electron transport ability of the catalyst material.

Herein, we report the synthesis of a self-supported core-shell composite electrocatalyst (NiP-FeP_2/NPC) for efficient overall water splitting using an *in situ* low-temperature phosphorylation reaction with $NiMoO_4$ as the precursor through a heterogeneous interface structure construction strategy. The homogeneous $NiMoO_4$ nanorod arrays provide a more reactive site and electron transport channel toward the nickel foam substrate. The disordered particles are embedded in carbon protection layers, which are suitable for the reactants entering the interior and improve stability during the harsh operating environment. From the above advantages, NiP-FeP_2/NPC/NF exhibits excellent catalytic performance in alkaline solutions. DFT calculations reveal that electrons aggregate and redistribute at the heterogeneous interface, effectively optimizing the adsorption of intermediates and reducing the Gibbs free energy, thus accelerating the catalytic process. The assembled solar-driven water-splitting system demonstrated a high and stable solar-to-hydrogen efficiency of 18.20%. This work provides a valuable strategy for developing non-noble metal-based bifunctional electrocatalysts for large-scale hydrogen production applications.

Fig. 1a illustrates the fabrication process of the NiP-FeP_2/NPC/NF catalyst. (For the reader's convenience, the writing of $NiMoO_4$ will be omitted below.) The target NiP-FeP_2/NPC structure is synthesized *via* annealing precursors under an Ar atmosphere. The $NiMoO_4$ nanorods are homogeneously distributed and vertically grown on nickel foam, which provides more active sites and forms a modified nanorod array (Fig. S1 in Supporting information). SEM images show that the homogeneous square pillar-shaped nanorod arrays are maintained throughout the synthetic process. After loading N, P-doped carbon layers (NPC), the morphology of the $NiMoO_4$ matrix is well retained. The roots of these pillars diameter of the nanorods, the most minor constituent units of the NiP-FeP_2/NPC, is approximately 350 nm (Fig. 1b and Figs. S1d–f). The SEM images of the NiMoO precursors, $NiMoO_4$/NPC/NF, and different inks coated with NiP/NPC/NF and FeP_2/NPC/NF are shown in Figs. S2 and S3 (Supporting information).

Further characterization by TEM confirms that the compositional nanorod possesses a typical pillar-like character with an inner diameter of approximately 300 nm and thin NPC layers about 3 nm thick (Figs. 1c and d), demonstrating that this heterogeneous structure is suitable for the reactants entered into the interior and suppressing the oxidation and aggregation of the NiP-FeP_2/NPC/NF nanorods. The apparent lattice spacing of 0.211 nm shown in the local magnified image could correspond to the (121) crystal plane

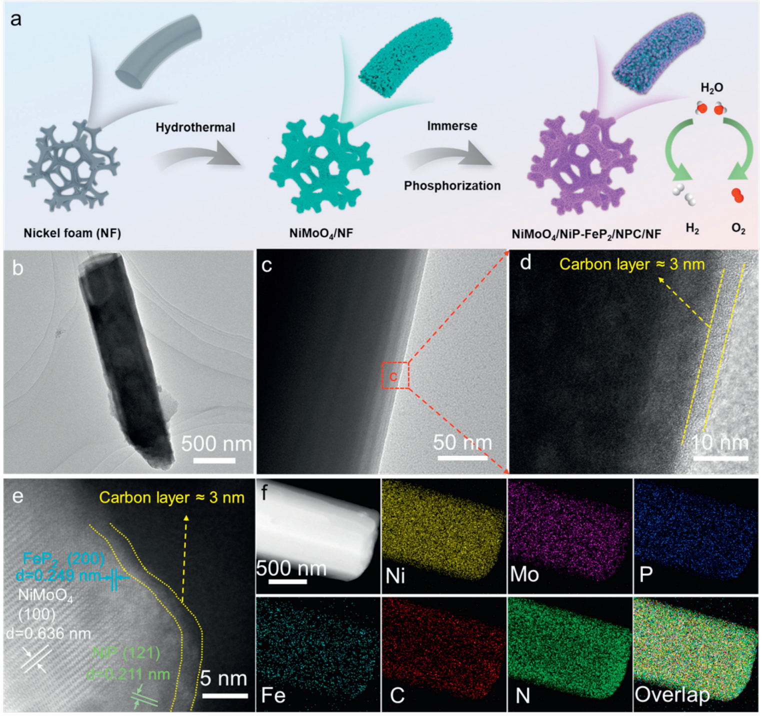

Fig. 1. (a) Schematic diagram of catalyst preparation. (b-e) TEM image and HRTEM image of NiP-FeP_2/NPC/NF. (f) HAADF-STEM image and EDS mapping of the NiP-FeP_2/NPC/NF catalyst.

of the NiP. The lattice spacing of 0.249 nm could correspond to the (200) crystal plane of FeP_2 (Fig. 1e). The two inlaid particle structures are arranged in a disorderly manner but are uniformly embedded into the covering layer. Under the successive synthesis process, separate square columnar arrays were retained, as well as NPC layers that protected the heterogeneous structure, which we expect will contribute to the long-term maintenance of efficient electrocatalytic activity in harsh catalytic environments. The high-angle annular dark-field scanning TEM (HAADF-STEM) images and the corresponding EDX mapping images reveal that the six elements Ni, Mo, Fe, P, N, and C are uniformly distributed over the pillar-like NiP-FeP_2/NPC heterogeneous nanorods (Fig. 1f). The prepared NiP-FeP_2/NPC heterogeneous nanorod arrays have unique features and multidimensional electron transport pathways, supporting the above results, which in part explain the excellent catalytic performance of the catalysts.

The XRD and XPS were conducted to investigate the crystal structure and surface components of the prepared FeP_2/NPC/NF, NiP/NPC/NF, and NiP-FeP_2/NPC/NF catalysts. As depicted in Fig. 2a, the peaks at 10.8°, 13.6°, 21.5°, 26.9°, 27.5°, and 33.2° correspond to the (001), (010), (102), (211), (200), and (022) crystal planes of $NiMoO_4$ host materials (PDF #33–0948), respectively. Except for the diffraction peak of $NiMoO_4$ and pure nickel, the peak of NiP-FeP_2/NPC/NF shows the presence of (111), (102), (122), (302) crystal planes of NiP (PDF #04–007–0813) at 26.7°, 29.8°, 48.1°, 52.5°, and (110), (020), (210), (031), (002) crystal planes of FeP_2 (PDF#04–003–1993) at 23.8°, 31.6°, 39.6°, 59.5°, and 68.9° The broad peak is seen near 24°, which confirms the formation of disordered carbon layer features. Compared to the XRD patterns of other obtained catalysts, the different inlaid particle materials show only small differences between peaks.

As depicted in Fig. S4 (Supporting information), the elements Ni, Fe, Mo, N, and P were probed in the XPS survey spectrum in accordance with the EDS results above. In Fig. 2b, the positions of the two main peaks are located at 856.1 eV and 870.2 eV, which can correspond to Ni $2p_{3/2}$ and Ni $2p_{1/2}$, respectively, and they can be deconvoluted into several smaller peaks that can correspond to Ni^{2+} and Ni^{3+} with a clear peak of 852.9 eV coming from the Ni-P bond [33–36]. In the Fe 2p patterns, the two peaks at 710.4 eV and 723.5 eV correspond to Fe $2p_{3/2}$ and Fe $2p_{1/2}$, and they can be deconvoluted into several smaller peaks, which correspond to Fe^{2+}, Fe^{3+}, and two satellite peaks (715.2 eV and 729.5 eV), and the distinct peak at 707.1 eV originates from the Fe-P bond (Fig. 2c) [37–42]. Moreover, as shown in Fig. 2d, the XPS pattern of Mo 3d was deconvoluted into four peaks at Mo^{4+} $3d_{5/2}$, Mo^{4+} $3d_{3/2}$, Mo^{6+} $3d_{5/2}$, and Mo^{6+} $3d_{3/2}$ with binding energies at 230.5 eV, 233.7 eV, 232.4 eV, and 235.5 eV, respectively [43–47]. In Fig. 2e, the N 1s XPS spectra are divided into three peaks of pyridinic N at 395.1 eV, pyrrolic N at 398.3 eV, and graphitic N at 400.8 eV, which also confirm the successful formation of N-doped carbon and the improved electric conductivity from the introduced additional electrons to the carbon material [48,49]. Two peaks at 129.3 eV and 130.4 eV in Fig. 2f are ascribed to P $2p_{3/2}$ and P $2p_{1/2}$, which can be well explained by the peak at 134.0 eV corresponding to the phosphorus-oxygen bond (P-O) due to the exposure of the sample to air [50–53].

In Fig. 3a, NiP-FeP_2/NPC/NF exhibited better HER performance compared with other samples when the current density was at 10 mA/cm^2. After fitting the LSV curve, the Tafel slope of NiP-FeP_2/NPC/NF is 77.8 mV/dec, which is lower than that of $NiMoO_4$/NPC/NF (133.8 mV/dec), NiP/NPC/NF (111.5 mV/dec), and FeP_2/NPC/NF (102.7 mV/dec), indicating faster reaction kinetics (Fig. 3b). In Fig. 3c, the overpotentials at specific values (10 and 100) of current density are counted for a more in-depth assessment of the catalyst's performance. The NiP-FeP_2/NPC/NF catalyst required only 59, 198, and 248 mV overpotential to achieve 10, 100, and 200 mA/cm^2 current densities, which were much lower than those of FeP_2/NPC/NF (122, 240, and 292 mV), NiP/NPC/NF (134, 260, and 320 mV) and $NiMoO_4$/NPC/NF (170, 293, and 349 mV). In Fig. 3d, Nyquist plots plotted by electrochemical impedance spectroscopy (EIS) testing showed that the NiP-FeP_2/NPC/NF catalyst had a charge transfer resistance (R_{ct}) of 0.2 Ω, the lowest of all samples, indicating the fastest charge transfer rate, in accordance with the results obtained from previous Tafel slope fit and polarization curve measurements (equivalent circuit shown in Fig. S17 in Supporting information).

In Figs. 3e and f, the long-term stability of the NiP-FeP_2/NPC/NF catalyst was evaluated *via* multiple testing methods. No distinct current attenuation was recorded when the chronoampere curve was measured for 20 h, and the potential shift was negligible after 5000 CV cycles. The result indicates that the NiP-FeP_2/NPC/NF catalyst has excellent stability. In addition, all samples were subjected to CV cycling at different scan rates under the non-Faraday region of the HER (Fig. S5 in Supporting information) to calculate the electrochemical double layer capacitance (C_{dl}). The results are shown in Fig. 3g. The value of NiP-FeP_2/NPC/NF is 13.35 mF/cm^2 and is larger than those of NiP/NPC/NF (9.77 mF/cm^2), FeP_2/NPC/NF (6.82 mF/cm^2), and $NiMoO_4$/NPC (3.01 mF/cm^2), fur-

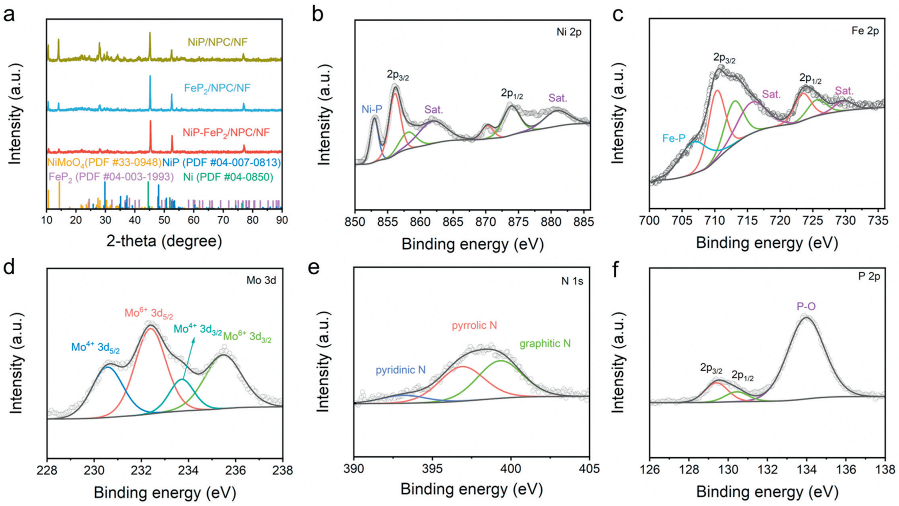

Fig. 2. (a) XRD patterns of as-synthesized catalysts. (b-f) High-resolution XPS spectra of Ni 2p, Fe 2p, Mo 3d, N 1s, and P 2p for NiP-FeP_2/NPC/NF.

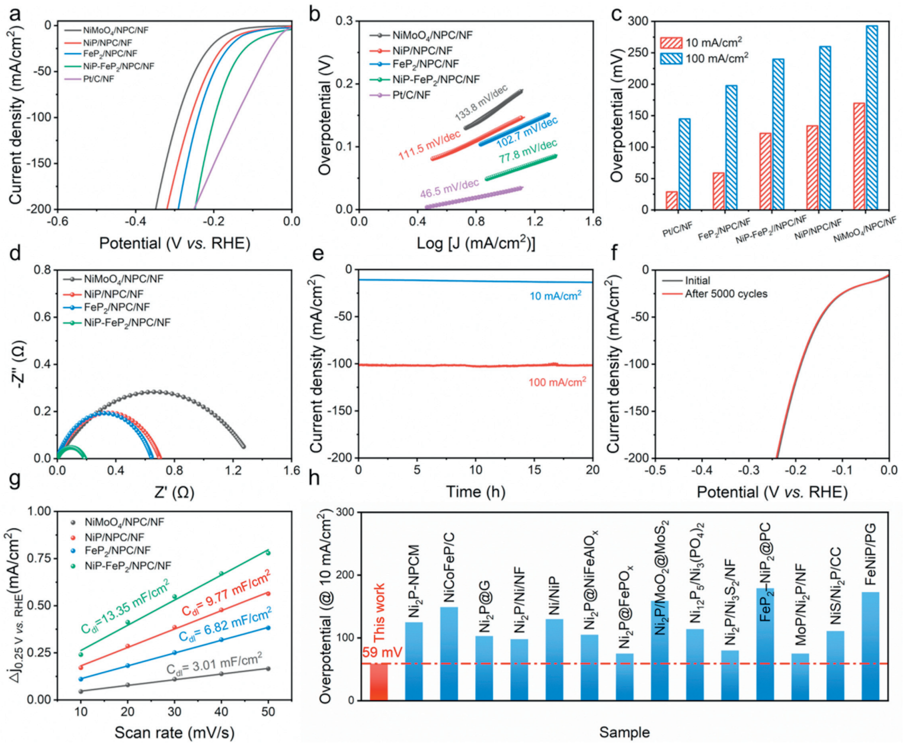

Fig. 3. (a) Polarization curves, (b) Tafel slopes, (c) overpotentials, (d) EIS Nyquist plots, (e) chronoamperometry curve of NiP-FeP$_2$/NPC/NF recorded for 20 h at 10 and 100 mA/cm^2. (f) Polarization curves of NiP-FeP$_2$/NPC/NF before and after stability testing. (g) Double-layer capacitances. (h) Overpotential at 10 mA/cm^2 of different catalysts.

ther indicating that the modified nanorod arrays did promote the exposure of the active sites, resulting in the increased catalytic activity of HER. The NiP-FeP$_2$/NPC/NF catalyst also exhibits better catalytic activity than the previously reported Ni-based HER catalysts due to their lower overpotential (Table S1 in Supporting information and Fig. 3h). The structural integrity of the NiP-FeP$_2$/NPC/NF catalyst was investigated by SEM and XPS measurements after the stability test. The catalyst showed a positive shift of about 0.6 eV for Ni 2p and a positive shift of about 1.3 eV for Fe 2p, indicating that the Fe atoms were partially oxidized (Figs. S6 and S7 in Supporting information). Meanwhile, the P 2p spectra and Mo 3d spectra were almost consistent before and after the HER reaction; both results demon- strate that the NiP-FeP$_2$/NPC/NF catalysts have good stability to sustain the HER reaction. The above results indicate that the prepared NiP-FeP$_2$/NPC/NF catalysts have superior catalytic activity and stability for HER.

In Fig. 4, the OER performance of the NiP-FeP$_2$/NPC/NF catalyst in the alkaline electrolyte was evaluated. Fig. 4a depict the LSV curves of various catalysts, which reveal that NiP-FeP$_2$/NPC/NF catalysts have the highest OER catalytic activity among all tested materials. The Tafel slope of NiP-FeP$_2$/NPC/NF catalysts is 44.3 mV/dec, which is lower than that of NiP/NPC/NF (52.8 mV/dec), FeP$_2$/NPC/NF (53.7 mV/dec), NiMoO$_4$/NPC/NF (54.8 mV/dec) and RuO$_2$ (59.8 mV/dec) and indicates favorable and fast OER kinetics in Fig. 4b. In Fig. 4c, the overpotentials required for the prepared NiP-FeP$_2$/NPC/NF catalysts at 10, 100, and 200 mA/cm^2 current densities are 187, 247, and 275 mV, respectively, which are much smaller than those of NiP/NPC/NF (205, 260, and 284 mV), FeP$_2$/NPC/NF (236, 303, and 334 mV), NiMoO$_4$/NPC/NF (254, 304, and 321 mV), and commercial RuO$_2$ (270, 341, and 380 mV) catalysts. The R_{ct} of NiP-FeP$_2$/NPC/NF catalyst is the smallest of all samples, suggesting a favorable charge transfer rate and fast OER kinetics (Fig. 4d). The synergistic effect between the NiMoO$_4$/NPC/NF nanoarray and the surface NiP-FeP$_2$ layer can significantly reduce the overpotential of the NiP-FeP$_2$/NPC/NF catalyst. The NiP-FeP$_2$/NPC/NF catalyst outperforms most recently reported Ni-based OER catalysts due to its lower overpotential and Tafel slope (Fig. 4h and Table S2 in Supporting information).

Similar to HER, NiP-FeP$_2$/NPC catalyst stability was characterized by the 20 h chronocurrent curve at a current density of 10 mA/cm^2 and 100 mA/cm^2. It was found that the current density was stable, showing no notable attenuation (Fig. 4e), indicating excellent long-term stability. In addition, stability can be evaluated by CV cycles, and the potential shifts that occur before and after 5000 cycles were negligible (Fig. 4f). The CV cycles with different scanning rates of different catalysts in the non-Faradic zone of OER were tested (Fig. S8 in Supporting information), and the C_{dl} was calculated. The capacitance value of the NiP-FeP$_2$/NPC/NF catalyst at 177.37 mF/cm^2 is greater than that of NiP/NPC/NF (80.96 mF/cm^2), FeP$_2$/NPC/NF (73.9 mF/cm^2), and NiMoO$_4$/NPC/NF (54.57 mF/cm^2) in Fig. 4g. It further shows that the heterostructure formed by the NiMoO$_4$ nanorod array and homogeneous ink under high-temperature phosphating creates abundant active sites, improving the OER catalytic activity. After the stability test, the catalysts were characterized by SEM and XPS; the results are shown in Figs. S9 and S10 (Supporting information). There were no significant changes in the surface morphology of the NiP-FeP$_2$/NPC/NF catalysts. In Fig. S10, the binding energy of Ni 2p shows a positive shift of about 0.8 eV, and the binding energy of Fe 2p shows a positive shift of about 1.8 eV, indicating that the Fe atom is oxidized. The P 2p and Mo 3d spectra were almost consistent before and after the OER reaction; both results demonstrate that the NiP-FeP$_2$/NPC/NF catalysts have good stability to sustain the OER reaction. The above results indicate that the prepared NiP-FeP$_2$/NPC/NF catalysts have superior catalytic activity and stability for OER.

As shown in Fig. 5a, the two-electrode electrolyzer (NiP-FeP$_2$/NPC/NF||NiP-FeP$_2$/NPC/NF) requires only 1.48 V to achieve a specific current density (10 mA/cm^2), which is much lower than

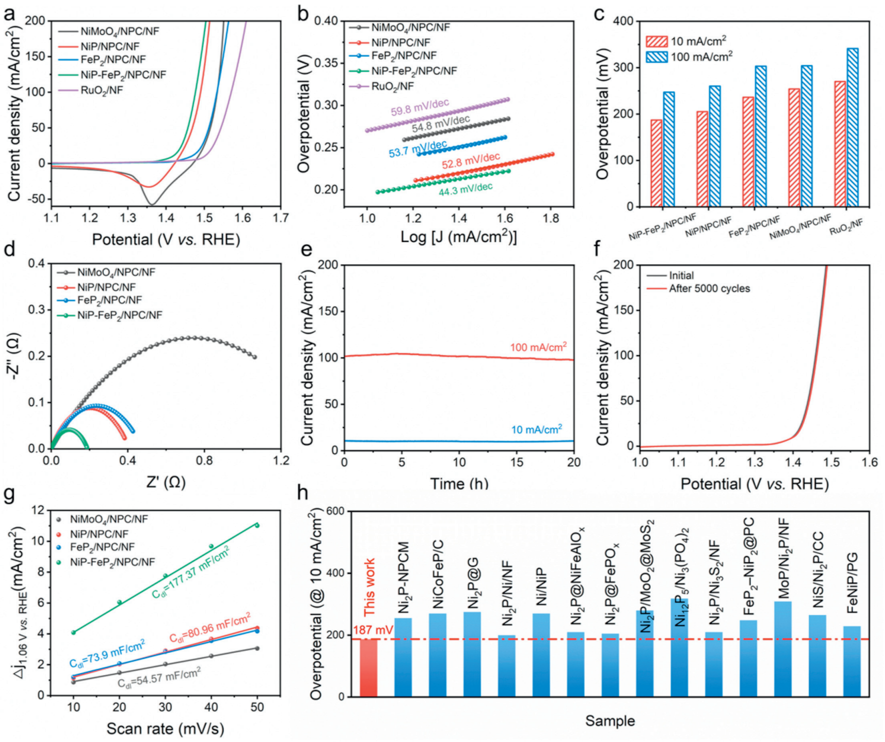

Fig. 4. (a) Polarization curves, (b) Tafel slopes, (c) overpotentials, (d) EIS Nyquist plots, (e) chronoamperometry curve of NiP-FeP_2/NPC/NF recorded for 20 h at 10 and 100 mA/cm^2. (f) Polarization curves of NiP-FeP_2/NPC/NF before and after stability testing. (g) Double-layer capacitances. (h) Overpotential at 10 mA/cm^2 of different catalysts.

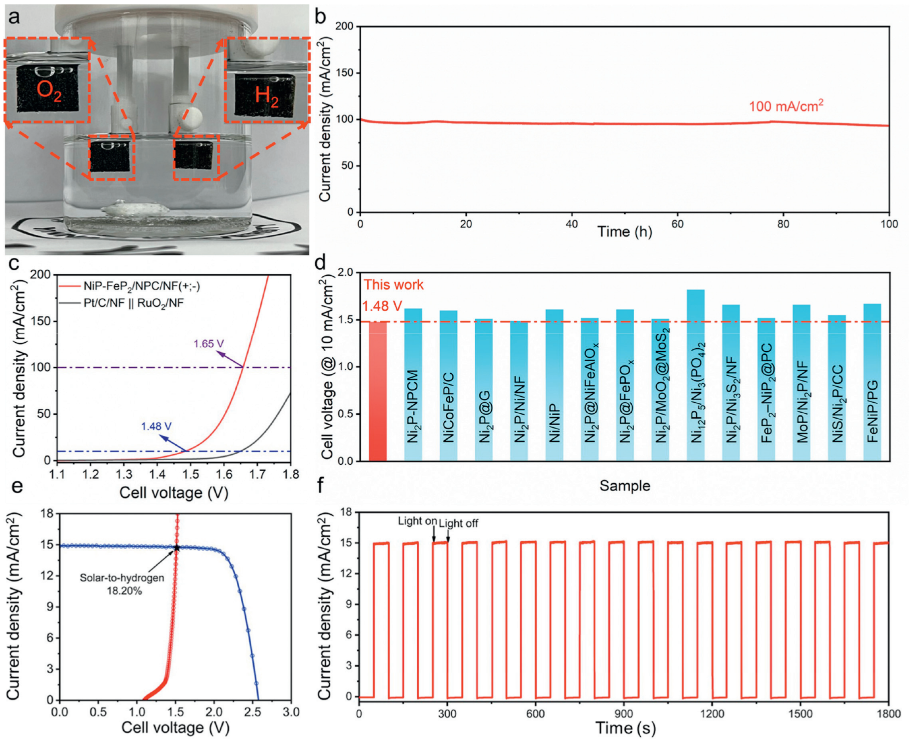

Fig. 5. (a) Photograph of NiP-FeP_2/NPC/NF electrolyzer. (b) Chronopotentiometry curve of NiP-FeP_2/NPC/NF. (c) Polarization curves in 1 mol/L KOH with 90% iR correction. (d) The cell voltage of different catalysts. (e) *J-V* curves of the solar-driven water-splitting electrolyzer. (f) The photocurrent response curve of the solar-driven water-splitting electrolyzer.

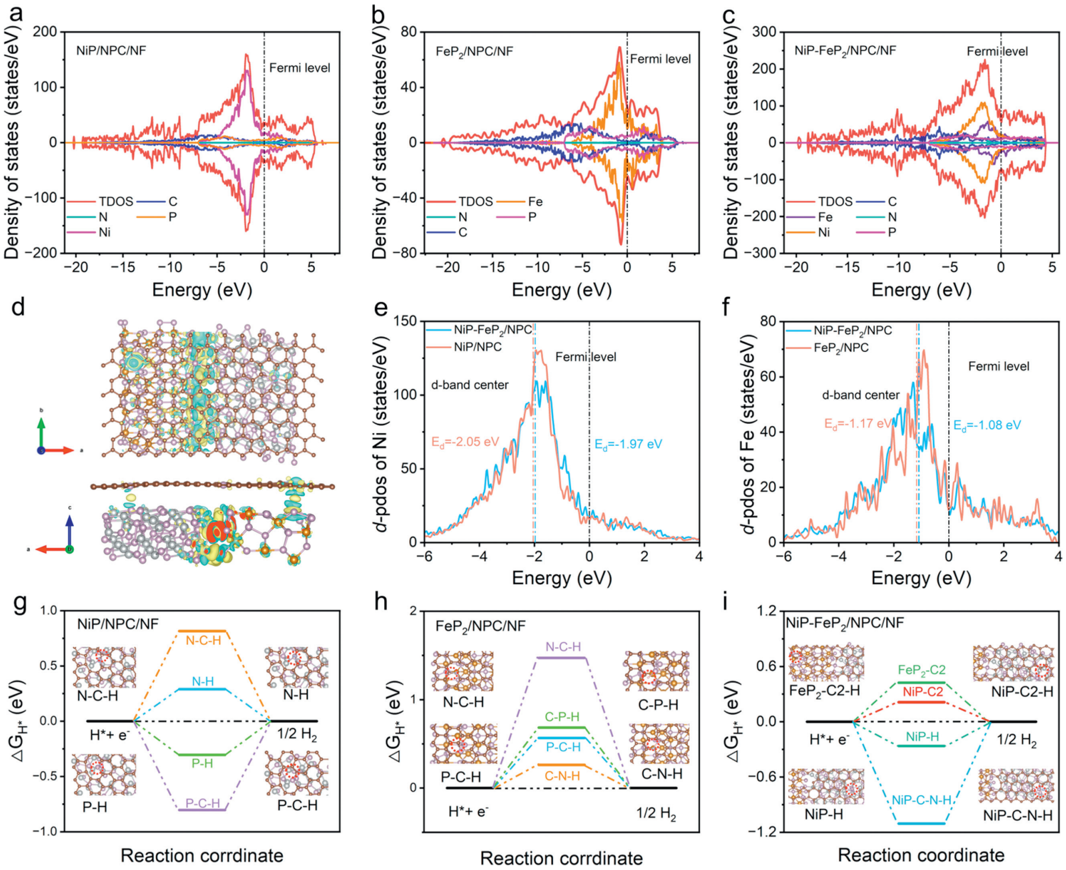

Fig. 6. (a-c) DOS of different samples. (d) Charge density distribution images of NiP-FeP$_2$/NPC. The d-band center of (e) Ni atoms and (f) Fe atoms in different samples. (g-i) Gibbs free energy diagrams for different sites in different samples.

the Pt/C/NF||RuO$_2$/NF couple (Fig. 5c). This activity outperforms many recently reported TMP-based electrocatalysts for water splitting (Fig. 5d and Table S3 in Supporting information). Long-term stability tests showed that NiP-FeP$_2$/NPC/NF could maintain a current density of 100 mA/cm^2 for 100 h with no activity decay (Fig. 5b). Moreover, when integrated with a commercial GaAs solar cell to assemble a solar-driven electrolyzer, a high and durable solar-to-hydrogen (STH) conversion efficiency of 18.20% was obtained, indicating the potential for the use of NiP-FeP$_2$/NPC/NF to store intermittent energy (Fig. 5e). In Fig. 5f, the photocurrent responds reversibly to the on/off cycles of the illumination and maintains a constant maximum value during illumination, verifying the performance reliability of the light drive. The superior catalytic activity and stability of NiP-FeP$_2$/NPC/NF demonstrate that it can be used as an attractive bifunctional electrocatalyst for water splitting.

To provide a deeper insight into the intrinsic mechanism of NiP-FeP$_2$/NPC/NF, the electronic structure of the catalysts and the possible reaction mechanism were investigated by density functional theory (DFT) calculations. The density of states (DOS) of the NiP/NPC/NF, FeP$_2$/NPC/NF, and NiP-FeP$_2$/NPC/NF models indicate the electronic structure of C on the surface, and the intensity of the longitudinal coordinates of the DOS of the three models demonstrates that the composition of the NiP-FeP$_2$ heterogeneous interface is accompanied by the adjustment of the electronic structure of the surface NPC, which optimizes the ΔG_{H^*} of the HER (Figs. 6a–c). As shown in Fig. 6d, there is a large amount of charge accumulation at the heterogeneous interface, leading to a redistribution of charge and thus boosting effective charge transport. Furthermore, the electronic structure of NiP-FeP$_2$/NPC is varied compared to NiP/NPC and FeP$_2$/NPC, with the d-band center of the Ni and Fe atoms being positively shifted compared to the Fermi level (Figs. 6e and f). The above results indicate stronger adsorption of reaction intermediates on the catalyst, thus improving the catalytic activity of the catalyst.

The diverse active center site models for NiP/NPC and FeP$_2$/NPC were constructed (Figs. S11 and S12 in Supporting information), and their ΔG_{H^*} was calculated, and the results are shown in Figs. 6g and h. Both NiP/NPC and FeP$_2$/NPC with N as the active center outperformed the other models in terms of ΔG_{H^*}. All possible active centers of NiP-FeP$_2$/NPC for HER were also considered, and their ΔG_{H^*} was calculated (Figs. S13-S15 in Supporting information). As shown in Fig. 6i, the C site on the NPC encapsulated outside NiP (named NiP-C2-H) has the ΔG_{H^*} closest to zero (0.22 eV), which is superior to the other active center sites on the NiP-FeP$_2$/NPC model (Fig. S16 in Supporting information). This result suggests that C is the true active site of NiP-FeP$_2$/NPC. Moreover, the ΔG_{H^*} value of NiP-C2-H is also much lower than that of each site in the NiP/NPC and FeP$_2$/NPC models, which indicates that NiP-FeP$_2$/NPC has faster HER reaction kinetics [54–56], which is also consistent with the experimental results obtained.

In summary, we demonstrated a composite material in which arrays of square pillar-like NiMoO$_4$ nanorods coated with NPC layers are uniformly contained in numerous nested nanoparticle structures. The as-prepared NiP-FeP$_2$/NPC/NF catalyst exhibits outstanding electrocatalytic activity and long-term stability. Theoretical calculations reveal that the composition of the NiP-FeP$_2$ heterogeneous interface is accompanied by the adjustment of the electronic structure of the surface NPC, with the d-band center of the Ni and Fe atoms being positively shifted compared to the Fermi level. Electrons aggregate and redistribute at the heterogeneous interface, effectively optimizing the adsorption of intermediates and reducing the Gibbs free energy, thus accelerating the catalytic process. In particular, the assembled two-electrode solar-driven water electrolyzer demonstrates a high and stable solar-to-hydrogen efficiency of 18.20%. This work opens a new avenue for developing efficient and robust non-precious metal-based bifunctional catalysts for large-scale water-splitting applications.

Declaration of competing interest

The authors declare that they have no known competing financial interests or personal relationships that could have appeared to influence the work reported in this paper.

Acknowledgments

This work was financially supported by Yunnan Applied Basic Research Projects (Nos. 202001BB050006, 202201AT070095), and Scientific Research Fund Project of Yunnan Provincial Department of Education (No. 2023Y0262), Education Reform Research Project of Yunnan University (No. 2021Z06). Authors thank Advanced Analysis and Measurement Center of Yunnan University for the sample testing service.

Supplementary materials

Supplementary material associated with this article can be found, in the online version, at doi:10.1016/j.cclet.2023.109268.

References

[1] W.J. Kwak, D.Sharon Rosy, et al., Chem. Rev. 120 (2020) 6626–6683.
[2] R. Chulliyote, H. Hareendrakrishnakumar, M. Raja, et al., ChemistrySelect 2 (2017) 10484–10495.
[3] Y. Shi, B. Zhang, Chem. Soc. Rev. 45 (2016) 1529–1541.
[4] J. Wang, Y. Gao, H. Kong, et al., Chem. Soc. Rev. 49 (2020) 9154–9196.
[5] S. Anantharaj, S. Noda, V.R. Jothi, et al., Angew. Chem. Int. Ed. 60 (2021) 18981–19006.
[6] S. Liu, Z. Hu, Y. Wu, et al., Adv. Mater. 32 (2020) 2006034.
[7] J. Kibsgaard, I. Chorkendorff, Nat. Energy 4 (2019) 430–433.
[8] F. Dionigi, Z. Zeng, I. Sinev, et al., Nat. Commun. 11 (2020) 2522.
[9] W. Lin, Y. Zhang, D. Li, et al., Water Res. 198 (2021) 117146.
[10] H.B. Wu, B.Y. Xia, L. Yu, et al., Nat. Commun. 6 (2015) 6512.
[11] M. Zeng, Y. Li, J. Mater. Chem. A 3 (2015) 14942–14962.
[12] Z. Wu, J. Wang, R. Liu, et al., Nano Energy 32 (2017) 511–519.
[13] J. Balamurugan, T.T. Nguyen, D.H. Kim, et al., Appl. Catal. B: Environ. 286 (2021) 19909.
[14] L. Li, P. Wang, Q. Shao, et al., Chem. Soc. Rev. 49 (2020) 3072–3106.
[15] G. Yasin, S. Ibraheem, S. Ali, et al., Mater. Today Chem. 23 (2022) 100634.
[16] W. Yu, Z. Chen, Y. Zhao, et al., Nanoscale 14 (2022) 4566–4572.
[17] K. Chhetri, A. Muthurasu, B. Dahal, et al., Materials Today Nano 17 (2022) 100146.
[18] N. Logeshwaran, S. Ramakrishnan, S.S. Chandrasekaran, et al., Appl. Catal. B: Environ. 297 (2021) 120405.
[19] C. Rong, X. Shen, Y. Wang, et al., Adv. Mater. 34 (2022) 2110103.
[20] P. Zhai, M. Xia, Y. Wu, et al., Nat. Commun. 12 (2021) 4587.
[21] E. Vijayakumar, S. Ramakrishnan, C. Sathiskumar, et al., Chem. Eng. J. 428 (2022) 131115.
[22] B. Hammer, J.K. Nørskov, Surf. Sci. 343 (1995) 211–220.
[23] B. Hammer, J.K. Nørskov, Nature 376 (1995) 238–240.
[24] A.J. Medford, P.G. Moses, K.W. Jacobsen, et al., ACS Catal. 12 (2022) 9679–9689.
[25] E.J. Popczun, J.R. McKone, C.G. Read, et al., J. Am. Chem. Soc. 135 (2013) 9267–9270.
[26] P. Xiao, M.A. Sk, L. Thia, et al., Energy Environ. Sci. 7 (2014) 2624–2629.
[27] M.S. Faber, R. Dziedzic, M.A. Lukowski, et al., J. Am. Chem. Soc. 136 (2014) 10053–10061.
[28] P. Wang, X. Zhang, J. Zhang, et al., Nat. Commun. 8 (2017) 14580.
[29] H. Li, P. Wen, D.S. Itanze, et al., Adv. Mater. 31 (2019) 1900813.
[30] X. Ding, Y. Xia, Q. Li, et al., ACS Appl. Mater. Interfaces 11 (2019) 7936–7945.
[31] Y. Zhang, L. Sun, L. Bai, et al., Nano Res. 12 (2018) 607–618.
[32] T. Liu, A. Li, C. Wang, et al., Adv. Mater. 30 (2018) e1803590.
[33] Y. Jin, X. Yue, C. Shu, et al., J. Mater. Chem. A 5 (2017) 2508–2513.
[34] Y.Y. Chen, Y. Zhang, X. Zhang, et al., Adv. Mater. 29 (2017) 1703311.
[35] X. Wu, J. Chen, Z. Wen, ACS Sustain, Chem. Eng. 9 (2021) 13225–13232.
[36] L. Yu, Q. Zhu, S. Song, et al., Nat. Commun. 10 (2019) 5106.
[37] M. Liu, L. Yang, T. Liu, et al., J. Mater. Chem. A 5 (2017) 8608–8615.
[38] D. Mukherjee, P.M. Austeria, S. Sampath, ACS Energy Lett. 1 (2016) 367–372.
[39] H. Huang, C. Yu, J. Yang, et al., J. Mater. Chem. A 4 (2016) 16028–16035.
[40] Y. Yan, L. Thia, B.Y. Xia, et al., Adv. Sci. 2 (2015) 1500120.
[41] J. Duan, S. Chen, A. Vasileff, et al., ACS Nano 10 (2016) 8738–8745.
[42] J. Xu, D. Xiong, I. Amorim, et al., ACS Appl. Nano Mater. 1 (2018) 617–624.
[43] S. Blomberg, N. Johansson, E. Kokkonen, et al., Materials (Basel) 12 (2019) 3727.
[44] S. Baoyi, X. Aiju, W. Jiang, Integr. Ferroelectr. 171 (2016) 16–22.
[45] X. Wu, J. Li, Y. Li, et al., Chem. Eng. J. 409 (2021) 128161.
[46] G. Solomon, A. Landström, R. Mazzaro, et al., Adv. Energy Mater. 11 (2021) 2101324.
[47] J. Ding, F. Li, J. Zhang, et al., J. Am. Chem. Soc. 145 (2023) 11829–11836.
[48] X. Huang, X. Xu, C. Li, et al., Adv. Energy Mater. 9 (2019) 1803970.
[49] R. Wang, X.Y. Dong, J. Du, et al., Adv. Mater. 30 (2018) 1703711.
[50] Y. Li, B. Wei, Z. Yu, et al., ACS Sustain. Chem. Eng. 8 (2020) 10193–10200.
[51] X. Wang, R. Tong, Y. Wang, et al., ACS Appl. Mater. Interfaces 8 (2016) 34270–34279.
[52] W. Zhang, Y. Liu, H. Zhou, et al., J. Mater. Sci. 54 (2019) 11585–11595.
[53] D. Jiang, Y. Xu, R. Yang, et al., ACS Sustain. Chem. Eng. 7 (2019) 9309–9317.
[54] J. Zhou, Y. Wang, X. Su, et al., Energy Environ. Sci. 12 (2019) 739–746.
[55] H. Zhang, H. Li, Y. Zhou, et al., J. Energy Chem. 77 (2023) 420–427.
[56] H. Zhang, Y. Zhou, M. Xu, et al., ACS Nano 17 (2023) 636–647.